



Theranostic Calcium Phosphate Nanoparticles With Potential for Multimodal Imaging and Drug Delivery

Madhumathi Kalidoss¹, Rubaiya Yunus Basha², Mukesh Doble² and T. S. Sampath Kumar^{1*}

¹ Medical Materials Laboratory, Department of Metallurgical and Materials Engineering, Indian Institute of Technology Madras, Chennai, India, ² Department of Biotechnology, Indian Institute of Technology Madras, Chennai, India

OPEN ACCESS

Edited by:

Hasan Uludag,
University of Alberta, Canada

Reviewed by:

Jonathan F. Lovell,
University at Buffalo, United States
Sergey V. Dorozhkin,
Independent Researcher, Moscow,
Russia

*Correspondence:

T. S. Sampath Kumar
tssk@iitm.ac.in

Specialty section:

This article was submitted to
Biomaterials,
a section of the journal
Frontiers in Bioengineering and
Biotechnology

Received: 13 February 2019

Accepted: 09 May 2019

Published: 04 June 2019

Citation:

Kalidoss M, Yunus Basha R, Doble M
and Sampath Kumar TS (2019)
Theranostic Calcium Phosphate
Nanoparticles With Potential for
Multimodal Imaging and Drug Delivery.
Front. Bioeng. Biotechnol. 7:126.
doi: 10.3389/fbioe.2019.00126

Calcium phosphate (CaP) bioceramics closely resemble the natural human bone, which is a main reason for their popularity as bone substitutes. However, this compositional similarity makes it difficult to distinguish CaPs, especially in particulate form, from native bone by imaging modalities such as X-ray radiography, computed tomography (CT), and magnetic resonance imaging (MRI) to monitor the healing progress. External contrast agents can improve the imaging contrast of CaPs but can affect their physicochemical properties and can produce artifacts. In this work, we have attempted to improve the contrast of CaP nanoparticles *via* ion substitutions for multimodal imaging. Calcium-deficient hydroxyapatite (CDHA) nanoparticles with silver (Ag), gadolinium (Gd), and iron (Fe) substitution were prepared by a microwave-accelerated wet chemical process to improve the contrast in CT, T1 (spin–lattice), and T2 (spin–spin) MRI relaxation modes, respectively. Ag, Gd, and Fe were substituted at 0.25, 0.5, and 0.25 at.%, respectively. The ion-substituted CDHA (ICDHA) was found to be phase pure by X-ray diffraction (XRD) and Fourier transform infrared spectroscopy (FT-IR). Transmission electron microscopy (TEM) images showed that the ICDHA nanoparticles were platelet shaped and of 52 ± 2 nm length and 6 ± 1 nm width. The ICDHA showed high contrast in X-ray and CT compared to CDHA. The vibrating sample magnetometry (VSM) studies showed the ICDHA to exhibit paramagnetic behavior compared to diamagnetic CDHA, which was further confirmed by improved contrast in T1 and T2 MRI mode. In addition, the *in vitro* tetracycline drug loading and release was studied to investigate the capability of these nanoparticles for antibiotic drug delivery. It was found that a burst release profile was observed for 24 h with 47–52% tetracycline drug release. The ICDHA nanoparticles also showed *in vitro* antibacterial activity against *Staphylococcus aureus* and *Escherichia coli* due to Ag, which was further enhanced by antibiotic loading. *In vitro* biocompatibility studies showed that the triple-ion-substituted ICDHA nanoparticles were cytocompatible. Thus, the ion-substituted CDHA nanoparticles can have potential theranostic applications due to their multimodal image contrast, antibacterial activity, and drug delivery potential. Future work will be conducted with actual bone samples *in vitro* or in animal models.

Keywords: multimodal imaging, calcium phosphate nanoparticles, drug delivery, antibacterial, image contrast, ion substitution, bone substitute, theranostics

INTRODUCTION

Calcium phosphate (CaP) bioceramics are one of the most commonly studied bone substitutes used for the repair of bony defects and alveolar ridge augmentation, as ear implants and as bone graft extender in spinal fusion surgery (Vallet-Regi and Gonzalez-Calbet, 2004; Habraken et al., 2016). Their popularity in bone therapeutic application is due to their compositional similarity to bone mineral as well as excellent biocompatibility and bioactivity (Sampath Kumar and Madhumathi, 2016b). CaP has also been used as delivery carriers for antibiotics, anti-inflammatory agents, anticancer drugs, growth factors, proteins, and DNA for bone tissue engineering due to its high drug loading ability (Uskokovic and Uskokovic, 2011). Hydroxyapatite (HA), calcium-deficient hydroxyapatite (CDHA), tricalcium phosphate (TCP), and biphasic calcium phosphate (BCP) are some of the popularly used CaPs.

A major drawback of CaPs, especially in nanoparticulate forms, is the difficulty in differentiating them from native bone tissue by imaging modalities such as X-ray radiography and computed tomography (CT) (Ramanathan and Ackerman, 1999; Ventura et al., 2014). It is essential to follow the stability of the implanted biomaterial, its infiltration by bone cells, the new bone formation and bone remodeling to optimize the performance of such bone substitutes. Imaging offers a non-destructive way of quantitative and longitudinal analysis of the above parameters. CaPs have nearly the same X-ray absorption as natural bone due to their compositional similarity to bone mineral. Other imaging modes such as magnetic resonance imaging (MRI) have not been utilized to image hard tissue like bone and synthetic CaPs, as it is exceedingly difficult to obtain MR signals due to the short spin-spin relaxation times of the nuclei (Wu et al., 1999). It has been observed that even at a high resolution, there is lack of contrast between surrounding bone and synthetic CaP bone substitute (Beaman et al., 2006). In order to enhance the imaging contrast of CaP bioceramics, addition of contrast agents

has been proposed. They include barium sulfate, tantalum oxide, strontium carbonate, gold, etc., for X-ray/CT imaging (Wang et al., 2007; Hoekstra et al., 2014; Mastrogiacomo et al., 2017) and gadolinium, iron, perfluorocarbon-based contrast agents, etc., for MR imaging (Wichlas et al., 2012; Mastrogiacomo et al., 2017; Nakamura et al., 2018). There are certain drawbacks associated with addition of such external contrast agents. For example, it has been shown that addition of CT and MRI contrast agents affects the setting time and mechanical properties of CaP and other bone cements (Tanomaru-Filho et al., 2012; Sun et al., 2013). Similarly, addition of external magnetic contrast agents like super paramagnetic iron oxide nanoparticles (SPIONS) can cause artifacts like blooming effects (Ventura et al., 2014).

Efforts toward improving the imaging of CaPs are currently focused on refining the current diagnostic techniques for better imaging and improving the inherent contrast of CaP bioceramics. Recent advancements in MRI are an example of the former approach. The development of ultra-short echo time and zero echo time techniques has made high-resolution bone imaging possible (Ventura et al., 2013; Dou et al., 2018). HA and other CaPs are highly amenable to functional modifications *via* ionic substitutions. Hence, toward the latter approach, contrast-enhanced CaPs have been developed by ionic substitutions (Qi et al., 2018). Since MRI and CT are two of the most common methods of imaging that, when combined together, can image both soft and hard tissues, it is very prudent to develop multimodal CT/MR contrast-enhanced CaP bioceramics.

Multimodal imaging refers to combining several imaging techniques by developing multifunctional contrast agents. Due to their multiple binding sites and functional groups, CaPs, in nanoparticulate form especially, have been widely tried as multimodal contrast agents for simultaneous diagnosis and therapeutic applications (nanotheranosis) (Qi et al., 2018). CaP nanoparticles have been used as contrast agents by conjugating with or encapsulating organic fluorophores, encapsulating gold nanoclusters, doping with elements [e.g., europium (Eu^{3+}), manganese (Mn^{2+}), gadolinium (Gd^{3+}), iron (Fe^{3+}), neodymium (Nd^{3+}), terbium (Tb^{3+}), dysprosium (Dy^{3+}), etc.], conjugating with quantum dots, radiolabeling with samarium (^{153}Sm), indium (^{111}In), lutetium (^{177}Lu), technetium ($^{99\text{m}}\text{Tc}$), etc., for imaging modalities including fluorescence, CT, MR, and nuclear imaging (Qi et al., 2018). HA nanoparticles exhibiting paramagnetism, near-infrared (NIR)

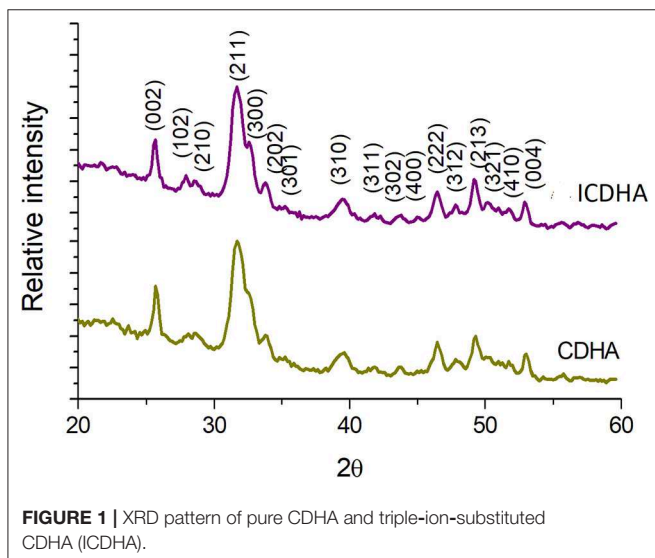


TABLE 1 | List of cell parameters, cell volume, and crystallite size obtained from XRD and TEM results.

Samples	Ion substitution (at.%)	Cell parameters (Å)		Cell volume (Å ³)	Crystallite size (nm)	
		a	c		XRD	TEM (L*W)
CDHA	–	9.371	6.862	505	31	(40 ± 3)*(5 ± 3)
ICDHA	0.25 Ag 0.5 Gd 0.25 Fe	9.470	6.860	533	49	(52 ± 2)*(6 ± 1)

fluorescence, and X-ray absorption by Eu^{3+} and Gd^{3+} doping have been developed by Ashokan et al. (2010). They had also developed CaP nanoparticles doped with both indocyanine green (ICG) and gadolinium (Gd^{3+}), and labeled with $^{99\text{m}}\text{Tc}$ -MDP for combined optical, magnetic, and nuclear imaging (Ashokan et al., 2013). The synthesis of Gd^{3+} -doped HA labeled with ^{153}Sm for serving as a dual-modal probe for SPECT and MRI is another example for multimodal imaging using CaPs (Liu et al., 2014). Modified CaPs with therapeutic agents can be used to achieve disease diagnosis by enhancing the imaging contrasts combined with chemotherapy/gene therapy/hyperthermia therapy (HTT)/photodynamic therapy (PDT)/radiation therapy (RT), etc. (Qi et al., 2018). For example, $\text{Eu}^{3+}/\text{Gd}^{3+}$ dual-doped HA have been used for simultaneous photoluminescent and magnetic imaging along with drug delivery application (Chen et al., 2011). Folic-acid-functionalized, Gd^{3+} -doped HA that functions as a theranostic system with MR imaging and production of $\text{HA-}^{159}\text{Gd-}^{32}\text{P}$ radioisotope by neutron activation for active targeting of osteosarcomas has been developed (Cipreste et al., 2016). Similarly, HA doped with both Fe^{2+} and Fe^{3+} ions has been developed for theranostic applications (Tampieri et al., 2012). The Fe-doped HA exhibited intrinsic magnetization and can be used for multiple applications including hyperthermia treatment as well to develop new magnetic ceramics for enhanced bone regeneration. Tseng et al. (2014) have reported that ^{111}In -labeled lipid CaP nanoparticles preferentially accumulated in the lymph nodes *via* lymphatic drainage, which were used for SPECT/CT imaging-guided lymphatic gene delivery.

In the current work, a multimodal CaP drug delivery system with intrinsic antibacterial activity and enhanced contrast for CT/MR imaging modalities has been attempted by ion substitution. The CDHA of Ca/P ratio 1.61 was chosen for triple ion substitutions based on our previous results where it was found to be superior to HA as a drug-releasing resorbable bone substitute for the prevention and treatment of bone infections (Madhumathi and Sampath Kumar, 2014). Our preliminary work has shown that silver and gadolinium substitution into the HA crystal structure has resulted in significant CT and T1 MR

contrast (Madhumathi et al., 2014). Iron (Fe^{3+}) with its large magnetic moments is used as a contrast agent in T2 relaxation mode of MRI (Chandra et al., 2012). Hence, the substitution of Fe along with Ag and Gd in CDHA for the additional T2 MR contrast will be studied. The contrast enhancement provided by the triple-ion-substituted CDHA nanoparticles will be characterized through X-ray, CT imaging, and MR imaging modes. In addition, the *in vitro* tetracycline loading and release profile, antibacterial activity, and biocompatibility of the substituted CDHA nanoparticles will also be evaluated.

MATERIALS AND METHODS

Materials

Analytical grade calcium nitrate $\text{Ca}(\text{NO}_3)_2 \cdot 4\text{H}_2\text{O}$, diammonium hydrogen phosphate $(\text{NH}_4)_2\text{HPO}_4$, silver nitrate $\text{Ag}(\text{NO}_3)$, gadolinium oxide Gd_2O_3 , ferric nitrate nonahydrate $\text{Fe}(\text{NO}_3)_3 \cdot 9\text{H}_2\text{O}$, and ammonia (30% GR) were purchased from MERCK, India. The drug tetracycline was purchased from Sigma Aldrich, India.

Synthesis of Pure CDHA Nanocarriers

Pure CDHA of Ca/P ratio 1.61 was prepared as reported earlier through a microwave-accelerated wet chemical reaction using $\text{Ca}(\text{NO}_3)_2 \cdot 4\text{H}_2\text{O}$ and $(\text{NH}_4)_2\text{HPO}_4$ as precursors (Siddharthan et al., 2004). The reaction was carried out at pH 10 using ammonia with stirring. The precipitate formed was subjected to microwave irradiation in a microwave oven (BPL India, 2.45 GHz, 800 W power) for 20 min, after which it was washed with distilled water and dried. The dried samples were then powdered using an agate mortar and pestle.

Synthesis of Triple-Ion-Substituted ICDHA Nanocarriers

The triple-ion-substituted CDHA was prepared by adding Ag, Gd, and Fe precursors along with $\text{Ca}(\text{NO}_3)_2 \cdot 4\text{H}_2\text{O}$ and $(\text{NH}_4)_2\text{HPO}_4$ using the same microwave-accelerated wet chemical method mentioned in the section Synthesis of Pure CDHA Nanocarriers. The amount of precursors was calculated by fixing Ag^+ concentration at 0.25 at.%, Fe^{3+} at 0.25 at.%, and Gd^{3+} at 0.5 at.%, restricting the total substitution to 1 at.%. The $(\text{Ca}+\text{Ag}+\text{Gd}+\text{Fe})/\text{P}$ ratios were maintained at 1.61. The sample was labeled as ICDHA.

Material Characterization

The phase and crystallinity of the nanocarriers were characterized by X-ray diffraction method (XRD, Bruker D8 DISCOVER, USA) using $\text{Cu K}\alpha$ radiation ($\lambda = 1.54 \text{ \AA}$). The diffraction patterns were recorded at a scanning rate of 1 step/s with a step size of $0.1^\circ/\text{step}$. The functional groups present in the CDHA and ICDHA nanocarriers were analyzed by Fourier transform infrared spectroscopy (FT-IR, Perkin-Elmer Spectrum Two, Germany) in the attenuated total internal reflectance (ATR) mode. The FT-IR spectra were collected from the range $4,000\text{--}510 \text{ cm}^{-1}$. The elemental composition of ICDHA was studied by scanning electron microscopy (SEM, FEI Quanta 200, Netherlands) using energy dispersive X-ray (EDS) analysis. The

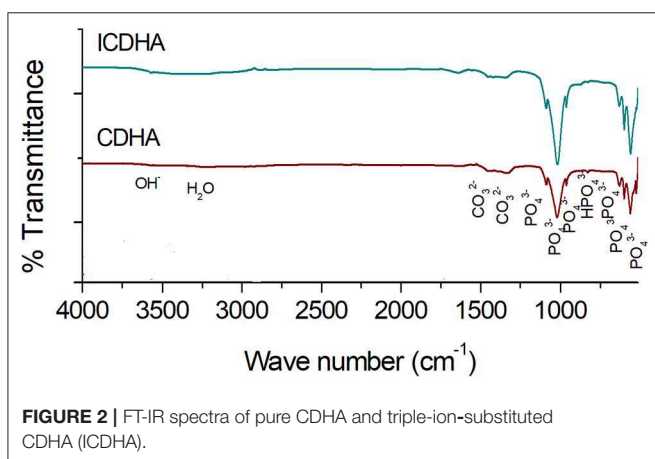


FIGURE 2 | FT-IR spectra of pure CDHA and triple-ion-substituted CDHA (ICDHA).

particles were dispersed in distilled water and ultrasonicated for 5 min. The dispersed nanoparticles were then sprayed on a cylindrical metal stub using an adhesive carbon tape. The surface was then dried and coated using gold for 2 min to improve the conductivity of the sample. Transmission electron microscopy (TEM, Philips CM20, Netherlands) was used to identify the size and morphology of the prepared nanocarriers. For TEM analysis, the apatite particles were dispersed in ethanol and ultrasonicated for 15 min. The dispersed samples were coated on carbon-coated copper grids, dried, and examined under TEM operated at 120 kV. The surface area measurements of the samples were obtained at the temperature of liquid nitrogen using the Brunauer–Emmett–Teller (BET) N_2 adsorption/desorption isotherm method (Sorptomatic 1990, USA). The magnetic properties of the nanocarriers were evaluated using vibrating sample magnetometry (VSM) at room temperature in an applied magnetic field of ± 1.5 T (Lakeshore VSM 7410, USA).

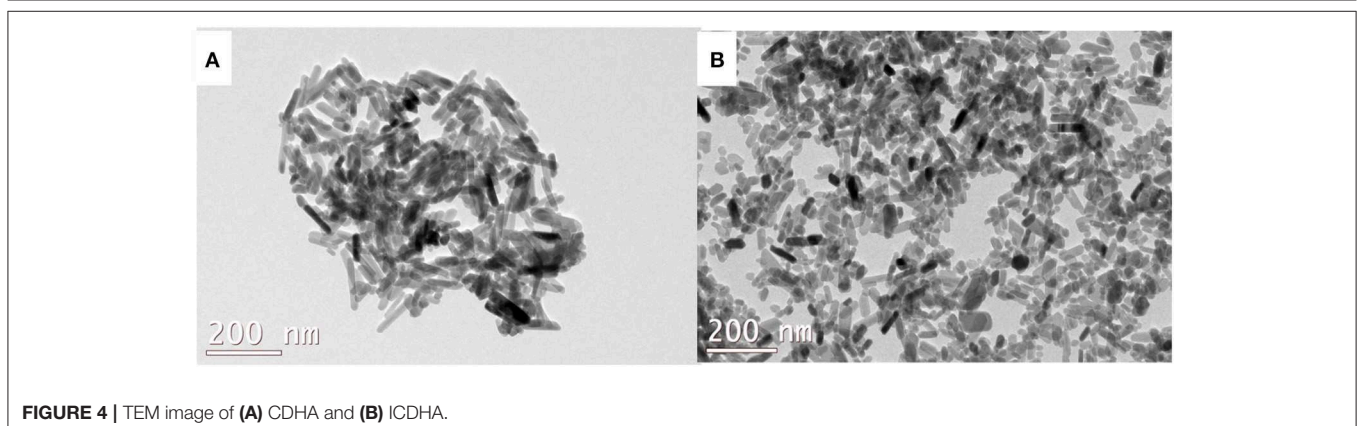
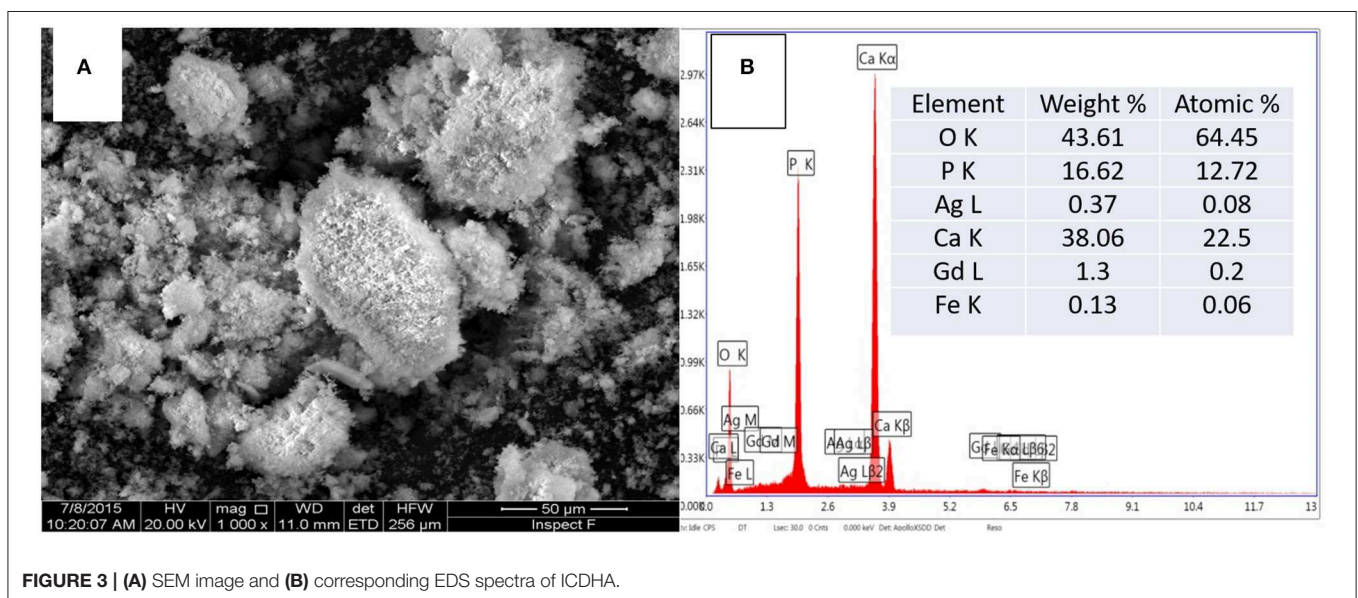
In vitro Imaging Studies

The image contrast properties of the ion-substituted samples were studied using radiography (X-ray) and CT imaging. The powder samples were weighed and compressed into pellets of

equal weight (200 mg) and 1 cm diameter. The X-ray radiographs were taken in a high-frequency X-ray generator (Siemens Multiphos 15, USA) along with aluminum standards of 1–5 mm thickness to differentiate the contrast. For CT scan, the pellets were placed inside a phantom model and imaged using a six-slice spiral CT (Philips Ingenuity Core128, USA) in a coronal section. For MR imaging, the nanocarriers were dispersed in distilled water. The MRI studies of triple-ion-substituted CDHAs were carried out by dispersing them in distilled H_2O at different concentrations (10–200 mM) and imaged in both T1 and T2 mode using a preclinical MR system (Bruker Biospec, France) of 4.7 T.

Drug Loading and Release

The drug loading and release studies were carried out from the ion-substituted samples using tetracycline following the procedure described earlier (Madhumathi and Sampath Kumar, 2014). About 5 mg of the drug was dispersed in 50 ml of suitable medium like ethanol or phosphate buffer solution (PBS). The CDHA and ICDHA nanocarriers (50 mg) were added to the drug-dispersed solution and placed in a constant temperature water bath at $37^\circ C$ for 24 h. After 24 h, 2 ml of supernatant was removed



for estimation of drug concentration using UV-Vis spectroscopy (Lambda 35, Perkin-Elmer, USA). The samples were centrifuged, filtered, and dried at room temperature for 24 h.

The amount of drug loaded onto the carriers was determined by the following equation:

$$\text{Drug loading \%} = (I_c - F_c) \div I_c \times 100 \quad (1)$$

Where I_c and F_c are the initial and final concentration of drug in PBS.

The release study was performed by dispersing 10 mg of drug-loaded carriers in 10 ml of PBS of pH 7.4. The samples were placed in a constant temperature water bath at 37°C. The concentration of drug released was estimated by removing 2 ml of supernatant and replaced by fresh PBS at various time intervals. The drug release profile was determined by measuring the absorbance values at different time intervals (F_c) from the initial loaded concentration (I_c). All the experiments were performed in triplicate.

In vitro Antibacterial Studies

The drug-loaded CDHA and ICDHA samples (10 mg) were added to 9 ml of nutrient broth. Pure and ion-substituted samples without drug were taken as controls. The suspensions were then inoculated with 1 ml of *Staphylococcus aureus* and *Escherichia coli* bacterial cultures and incubated at 37°C for 24 h with shaking. The antibacterial efficacy of the samples was determined from the optical density (OD) of the cultures at 600 nm using the following equation:

$$\text{Bacterial reduction \%} = \{1 - (\text{sample OD} \div \text{control OD}) \times 100\} \quad (2)$$

In vitro Biocompatibility Studies

The biocompatibility of the drug-loaded triple-ion-substituted nanoparticulate system was tested against Swiss 3T3 fibroblast cells (NCCS, Pune) by the colorimetric MTT [3-(4, 5-181dimethylthiazole-2-yl)-2,5-diphenyl tetrazolium bromide] assay for 48 h. The Swiss 3T3 fibroblast cells were grown to confluence with Dulbecco's modified Eagle's medium (DMEM) supplemented with 10% fetal bovine serum (FBS) and 1% 100× antibiotic-antimycotic liquid and incubated at 37°C with 5% carbon dioxide in a CO₂ incubator (Astec, Japan). The cells were then trypsinized and counted with a hemocytometer (Marienfeld, Germany). They were then diluted at 5,000 cells per well, seeded in 96-well plates, and cultured for 24 h. Ten milligrams of the samples was suspended in 1 ml of DMEM and incubated at 37°C for 24 h. The media in the 96-well plates was then replaced with 100 μl of the supernatant from the CDHA samples and again incubated for 24 h. Twenty microliters of 5 mg/ml MTT was added to each well and incubated for 4 h. The purple formazan precipitate formed selectively by live cells was solubilized in dimethyl sulfoxide (DMSO), and the absorbance was measured at 570 nm using a multimode plate reader (EnSpire, Perkin-Elmer, Singapore). The percentage of viable cells was calculated as the

percentage relative to the control (standard polystyrene tissue culture plates) using the following equation:

$$\text{Cell viability \%} = (\text{Sample OD} \div \text{Control OD}) \times 100 \quad (3)$$

Statistical Analysis

The values are expressed as mean ± SD. Statistical analysis was performed using one- and two-way ANOVA wherever applicable with a p -value < 0.05 considered statistically significant.

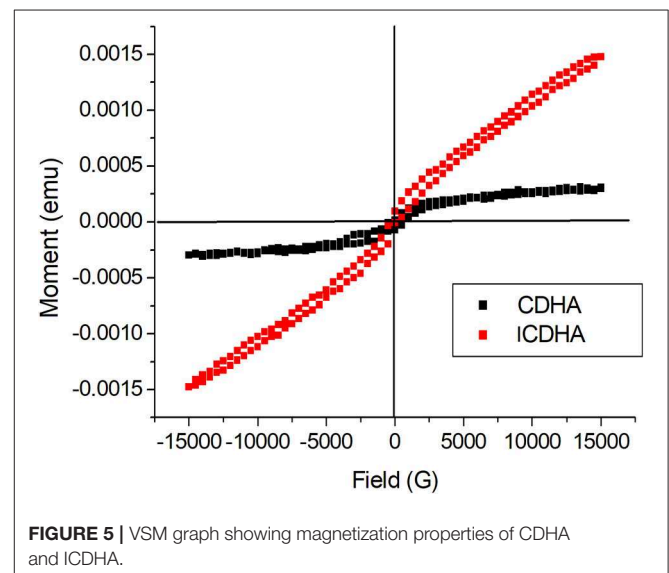
RESULTS

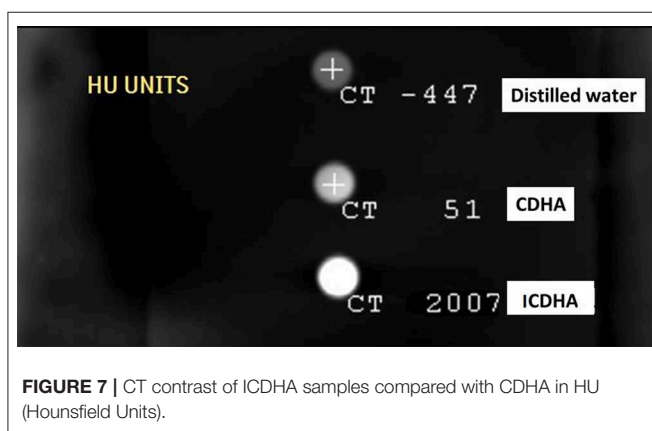
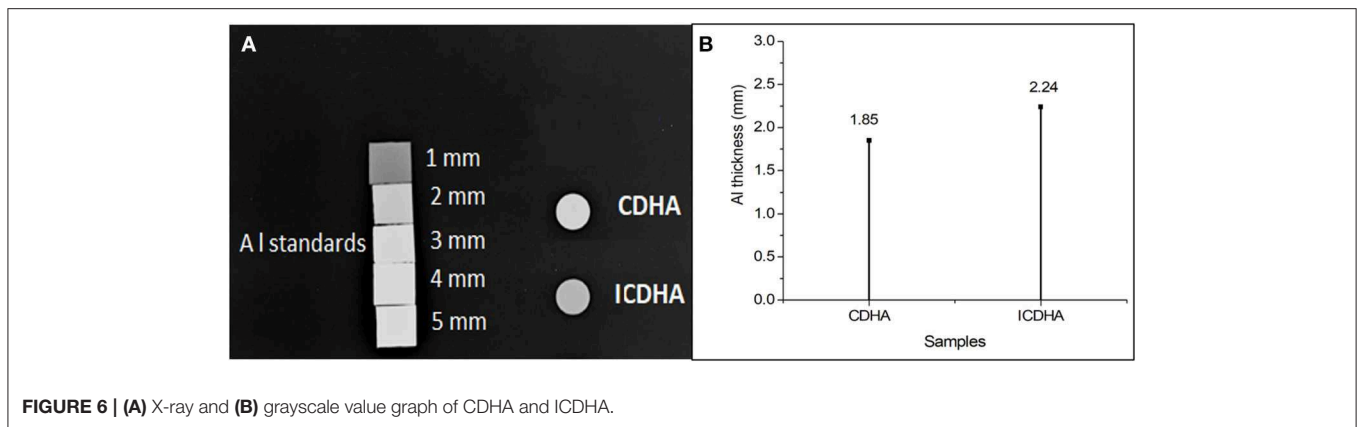
Material Characterization

The XRD pattern of pure CDHA and ICDHA is shown in **Figure 1**. The ion-substituted samples exhibit peaks similar to pure HA (JCPDS 09-432) and also revealed no secondary phases other than that of HA, suggesting ionic substitution in CDHA lattice. The cell parameters and cell volume calculated using "Unitcell" software and the crystallite size calculated using Scherrer's formula from XRD spectra are listed in **Table 1**. The ICDHA sample also showed larger cell parameters and a crystallite size of 49 nm when compared to pure CDHA with a crystallite size of 31 nm.

The FT-IR spectra of pure and triple-ion-substituted CDHA are shown in **Figure 2**. All the vibration bands of ion-substituted CDHA correspond to that of the characteristic bands of pure CDHA. The peaks observed include lattice OH (3,573 cm⁻¹); vibrational OH (634 cm⁻¹); phosphate bands at 470, 565, 603, 962, 1,035, and 1,090 cm⁻¹; carbonate (1,457 and 1,423 cm⁻¹); and lattice water (3,422 cm⁻¹). Additional HPO₄²⁻ peak at 874 cm⁻¹ was also observed from ion-substituted CDHA samples.

Figure 3 shows the SEM image and corresponding EDS spectra of ICDHA. It can be seen that ICDHAs appear as micron-sized aggregates in **Figure 3A**. The EDS spectra show the presence of Ag, Gd, and Fe in the samples in addition to Ca and P. The typical TEM images of triple-ion-substituted





samples can be seen in **Figure 4**. The TEM image of ICDHA samples showed large nanoparticles with acicular morphology. The particle sizes calculated from TEM micrographs using ImageJ image analysis software are listed in **Table 1**. The surface areas of CDHA and ICDHA samples from BET studies were 58 and 45 m²/g, respectively. **Figure 5** shows the results of VSM studies presenting the magnetization properties before and after ion substitutions in CDHA nanocarriers. It can very well be seen that the diamagnetic CDHA nanoparticles showed paramagnetic behavior on ion substitution.

X-ray, CT, and MR Imaging Studies

The X-ray radiographical image of the pellets of ICDHA in comparison to CDHA is shown in **Figure 6A**. It can be seen that the ICDHA pellet exhibited visibly higher contrast than pure CDHA. To further quantify the contrast (grayscale value), the pellets of the samples were compared along with aluminum (Al) standards of varying thickness (1–5 mm) as can be seen in **Figure 6A**. ImageJ software was used to quantify the grayscale value. **Figure 6B** shows the grayscale value graph corresponding to the X-ray image. The graph was obtained by plotting the contrast of the pellets (*x*-axis) with respect to the contrast of Al standards (*y*-axis). The graph shows that the contrast of ICDHA is comparable to that of

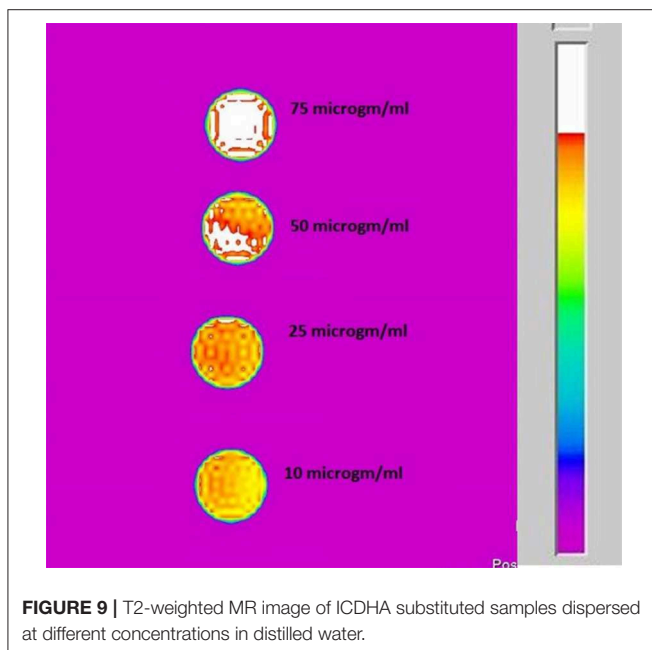
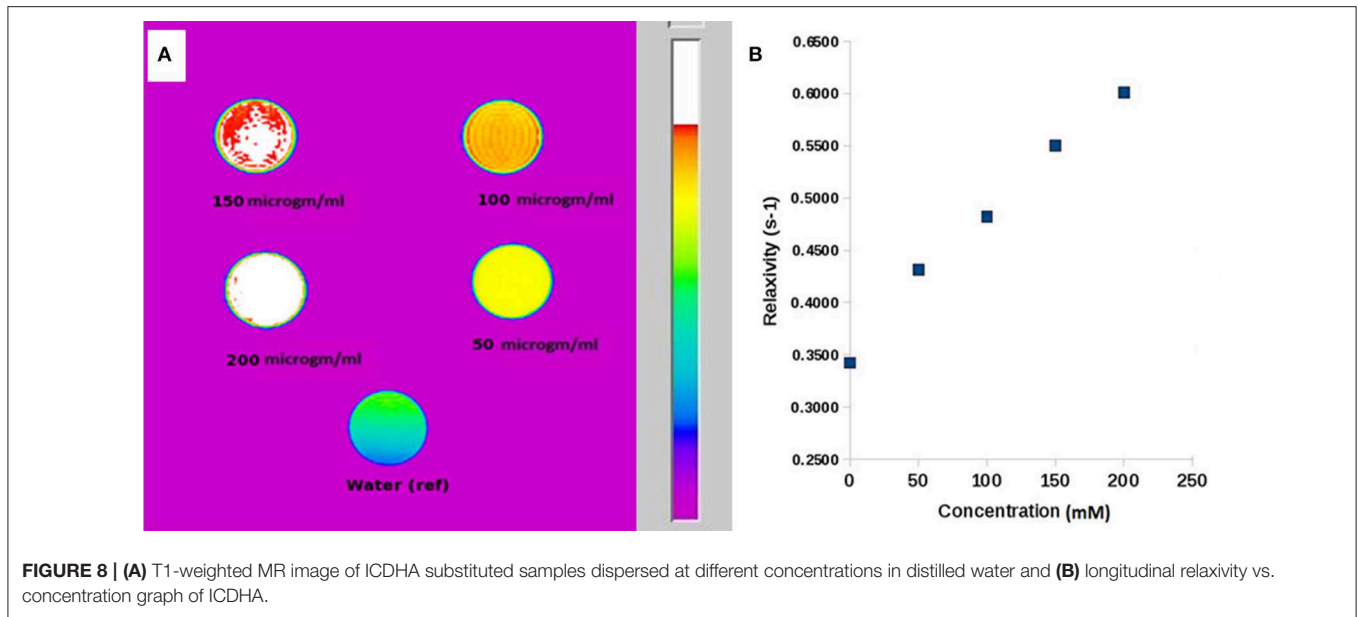
2.24 mm Al thickness while that of CDHA can be compared to 1.8-mm Al thickness. The substitution of elements with high density like Ag⁺ (10.49 g/cm³), Gd³⁺ (7.90 g/cm³), and Fe³⁺ (7.86 g/cm³) greatly increased the radiopacity of ICDHA compared to CDHA. The CT scan radiograph with ICDHA and CDHA samples is shown in **Figure 7**. The contrast values in CT are quantified in Hounsfield Units (HU). While both CDHA and ICDHA showed greater contrast than distilled water (control), ICDHA (2007 HU) exhibited much superior contrast than CDHA (51 HU).

The MR contrast images of ICDHA in T1 and T2 mode are shown in **Figure 8**. As observed in **Figure 8A**, the T1 MR contrast increased for the ICDHA samples with increasing concentrations. The color bar adjacent to the MR image shows the color change from bottom to top according to increase in contrast. Significant T1 contrast was observed at a concentration of 50 μg/ml and increased up to the concentration of 200 μg/ml. **Figure 8B** shows the concentration vs. longitudinal relaxivity (*r*₁) plot for ICDHA samples. The *r*₁ was calculated according to the equation:

$$(1 \div T_1)_{obs} = (1 \div T_1)_{dia} + r_1M \quad (4)$$

where $(1/T_1)_{obs}$ is the observed relaxation rate in the presence of ICDHA, $(1/T_1)_{dia}$ is the diamagnetic relaxation rate in the absence of nanoparticles, and *M* is the molar concentration (Ashokan et al., 2010). The T1 relaxivity increased with an increase in the ICDHA nanocarrier concentration. The maximum *r*₁ observed for ICDHA nanocarriers was 0.61 mM⁻¹ s⁻¹ for 200 μg/ml.

Figure 9 shows the T2 MR contrast for different concentrations of the ICDHA samples (10–200 μg/ml). The T2 images were obtained by pulse sequence spin-echo technique with TR/TE = 4,000/60 ms and FOV as 8 × 8 cm². Mild T2 contrast was observed at 10 μg/ml concentration and increased for up 75 μg/ml concentration with no further increase. The contrast obtained in T2 mode was much lower than that of the T1 mode, and so the T2 relaxivity graph was not plotted.



Drug Loading and Release Studies

The drug loading and release studies were carried out using the tetracycline antibiotic. **Figure 10** shows the drug loading percentage of ion-substituted apatites compared with pure samples. ICDHA showed a lower antibiotic loading (~40–55%) compared to CDHA (65–70%). This may be attributed to the lower surface area of ICDHA as well as due to the replacement of Ca^{2+} ions with other ions that might affect the drug binding.

The drug release profile of tetracycline from CDHA and ICDHA, however, looks similar (**Figure 11**). The ion substitutions caused a minor change in the drug release profiles.

The ICDHA samples showed a burst release of tetracycline with maximum release at 24 h, and the maximum release was lower than CDHA, which can be related to the changes in particle size as well as the non-stoichiometric nature of ion-substituted apatites.

In vitro Antibacterial Studies

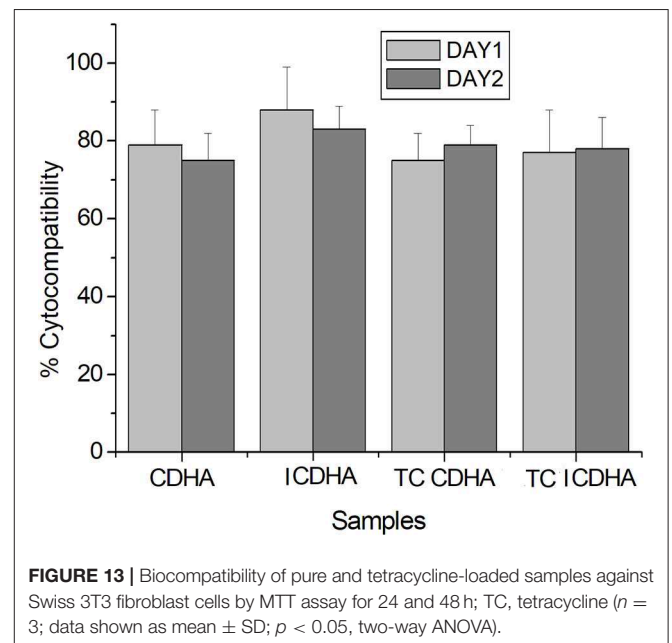
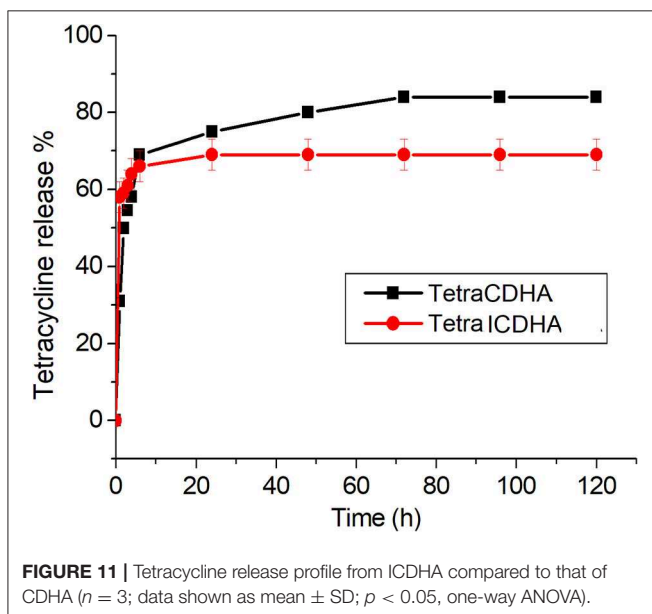
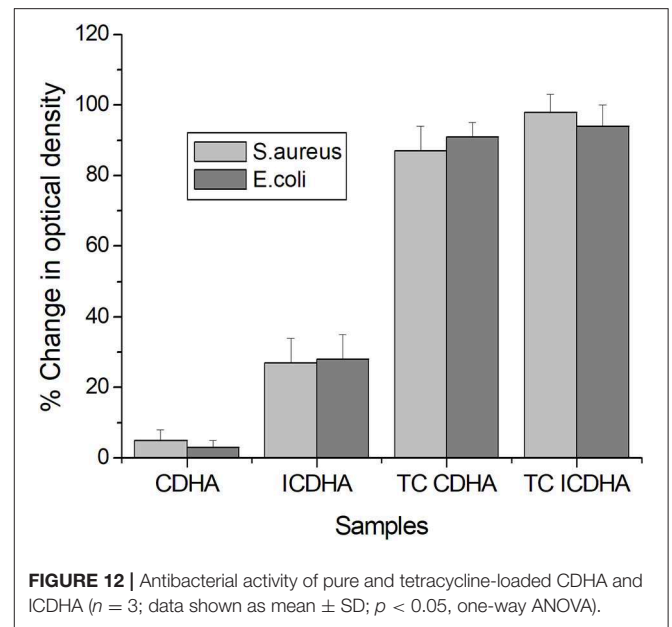
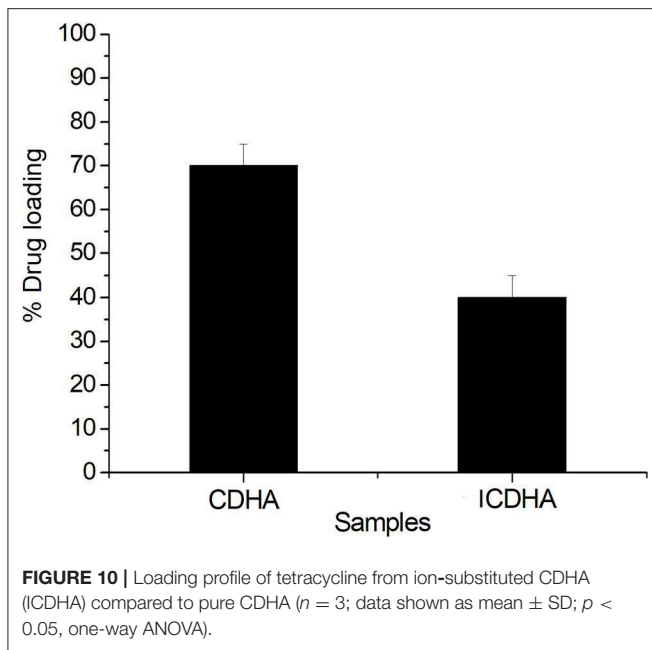
The results of the antibacterial studies of ion-substituted apatites against *S. aureus* and *E. coli* are shown in **Figure 12**. Although pure CDHA was not antibacterial, the ICDHA showed antibacterial activity between 20 and 25%, which can be attributed to the presence of Ag^+ . The antibacterial activity further increased with tetracycline loading as expected. All tetracycline-loaded samples showed >90% activity against both bacterial strains. The ion-substituted tetracycline-loaded ICDHA showed the highest antimicrobial activity against *S. aureus*, which is known to cause osteomyelitis and prosthetic joint infection when introduced through trauma, surgery, direct colonization from a proximal infection, or systemic circulation (Sampath Kumar and Madhumathi, 2016a).

In vitro Biocompatibility Studies

The MTT assay results of pure and drug-loaded ICDHA apatites on Swiss 3T3 fibroblast cells are shown in **Figure 13**. It can be seen that all samples including the antibiotic-loaded CDHA and ICDHA samples showed 80–100% cell viability on Day 1 and 75–85% cell viability on Day 2. The high cell viability in ion-substituted samples may be due to the low total ionic substitution of ~1%.

DISCUSSION

Regeneration and healing of bone tissue post trauma, surgery, or infection often require the implantation of a natural bone graft or synthetic bone substitute. While the ability to aid and promote new bone formation is the main emphasis in developing such



bone substitutes, it is also desirable to focus on other beneficial properties such as drug delivery ability, antibacterial activity, and optimal image contrast. In our previous studies, nanoparticulate bone substitutes with the abovementioned properties have been developed through approaches of drug loading and/or ion substitutions (Madhumathi and Sampath Kumar, 2014; Sampath Kumar et al., 2015). It was found that the substitution of ions such as Ag^+ , Gd^{3+} , etc. imparted antibacterial activity and greater image contrast in CT and T1 MR modes.

Conventional MRI contrast agents enhance contrast either in T1 mode (bright signal) or T2 mode (dark signal). Recent research in the field of MR imaging focuses on the challenge

to develop contrast agents that enhance both dual T1 and T2 MRI contrast. These T1/T2 contrast agents are designed for a single instrument and assumed to have advantages such as signal reliability and lack of image mismatch, which can occur when using different contrast agents or different instruments (Shin et al., 2015). An overlay of the T1 and T2 signals can help distinguish the targets from the surroundings. Dual T1/T2 imaging has been achieved through complex routes such as conjugation of T1 and T2 elements [e.g., covalently attaching Gd-DTPA with dopamine-coated iron oxide nanoparticles *via* isothiourea linkage, manganese (Mn)-embedded iron oxide

nanoparticles, etc.] and magnetically decoupled T1–T2 dual mode contrast agents [e.g., Mn-doped iron oxide (MnFe_2O_4) nanoparticles as the core T2 contrast material and $\text{Gd}_2\text{O}(\text{CO}_3)_2$ as the shell T1 contrast material separated by non-magnetic silica layer] (Bae et al., 2010; Choi et al., 2010; Huang et al., 2014). Since the apatitic structure allows for flexible ion substitution, we aimed to develop CDHA nanoparticles capable of simultaneous T1 and T2 MR contrast along with CT by substituting both Gd^{3+} and Fe^{3+} ions. One of the main criteria in deciding the percentage of Ag^+ , Gd^{3+} , and Fe^{3+} ion substitutions in CDHA was biocompatibility, and the total ion substitution was restricted to 1 at.%. Previous reports have shown that the Ag^+ and Gd^{3+} ion substitutions in HA have been found to be biocompatible at up to 0.5 and 4.4 at.%, respectively (Ramesh babu et al., 2007; Getman et al., 2010). Hence, the silver concentration was fixed at 0.25 at.%, the Gd^{3+} concentration was restricted to 0.50 at.% allowing Fe^{3+} substitution of 0.25 at.%, and the maximum combined substitution was restricted to 1 at.%.

The synthesized ICDHA samples were found to be phase pure as observed from XRD pattern and FT-IR spectra. The EDS spectra showed the presence of Ca, P, Ag, Gd, and Fe ions in the ICDHA samples. TEM image of ICDHA samples showed them to be of similar morphology but larger sized compared to CDHA. The ICDHA samples showed a greater X-ray and CT contrast than CDHA. ICDHA also showed a greater magnetic moment in VSM than pure CDHA. A dual T1/T2 imaging ability was observed with the ICDHA, although the contrast enhancement obtained in T1 mode was much higher than that in T2 mode. The relaxivity plot for the T2 mode was not obtained due to the low T2 contrast probably owing to the low at.% of Fe^{3+} substitution compared to Gd^{3+} . However, a dual T1/T2 contrast using very low ionic substitution was demonstrated. Drug delivery studies using tetracycline were performed to observe any modification in the antibiotic binding and release kinetics due to ion substitution in ICDHA. The studies showed a distinct reduction in the loading and a tendency toward burst release for these samples compared to pure CDHA. While the low loading may be attributed to the lower surface area of ion-substituted apatites and loss of Ca^{2+} binding sites, the burst release in ICDHA can be attributed to the release of drugs adsorbed on the surface. The antibacterial studies on *S. aureus* and *E. coli* showed a significant antibacterial activity of ICDHA due to Ag^+ even without antibiotic loading. With antibiotic binding, the antibacterial activity increased to >95%. Due to the low total ionic substitution of 1 at.%, both samples showed high biocompatibility for up to 48 h even with drug loading. Further *in vivo* studies can validate the above observations, suggesting that ICDHA

samples can act as biodegradable theranostic nanocarriers of antibiotics with inherent CT/T1/T2 MR contrast and antibacterial activity.

CONCLUSION

In the present study, ion-substituted CDHA nanoparticles with antibacterial activity and enhanced CT/T1/T2 MR image contrast for theranostic applications were developed. Ions such as Ag^+ , Gd^{3+} , and Fe^{3+} , which enhance contrast in CT, T1, and T2 MR modes, respectively, were substituted into the CDHA apatitic crystal structure. Preliminary results showed that the contrast enhancement in CT/T1/T2 MR modes was significant for a low amount of ionic substitution (0.25 at.% Ag^+ , 0.5 at.% Gd^{3+} , and 0.25 at.% Fe^{3+}). These multifunctional CDHA nanoparticles were inherently antibacterial due to Ag^+ substitution and also showed predominantly burst release of tetracycline antibiotic. The ion-substituted CDHA nanocarriers were also biocompatible due to the total ionic substitution of 1 at.%. The antibiotic-loaded triple-ion-substituted CDHA nanoparticles with antibacterial activity and multimodal image contrast are highly suitable for clinical orthopedic applications.

DATA AVAILABILITY

All datasets generated for this study are included in the manuscript and/or the supplementary files.

AUTHOR CONTRIBUTIONS

TS and MK conceived the idea. MK performed the material synthesis, characterization, drug release, and imaging experiments. RY planned and carried out the antibacterial and biocompatibility studies under the guidance of MD.

FUNDING

The study is funded by Department of Biotechnology, Govt. of India.

ACKNOWLEDGMENTS

We thank the Institute Hospital, Indian Institute of Technology Madras for providing the X-ray facility. We also thank Prof. N. Chandrakumar and Dr. Abhishek Banerjee of MRI-MRS Center, Department of Chemistry, Indian Institute of Technology Madras for help with the MR imaging.

REFERENCES

Ashokan, A., Gowda, G. S., Somasundaram, V. H., Bhupathi, A., Peethambaran, R., Unni, A. K. K., et al. (2013). Multifunctional calcium phosphate nano-contrast agent for combined nuclear, magnetic and near-infrared *in vivo* imaging. *Biomaterials* 34, 7143–7157. doi: 10.1016/j.biomaterials.2013.05.077

Ashokan, A., Menon, D., Nair, S., and Koyakutty, M. (2010). A molecular receptor targeted, hydroxyapatite nanocrystal based multi-modal contrast agent. *Biomaterials* 31, 2606–2616. doi: 10.1016/j.biomaterials.2009.11.113

Bae, K. H., Kim, Y. B., Lee, Y., Hwang, J., Park, H., and Park, T. J. (2010). Bio inspired synthesis and characterization of gadolinium labelled magnetite nanoparticles for dual contrast T1 and T2 weighted magnetic resonance imaging. *Bioconjugate Chem.* 21, 505–512. doi: 10.1021/bc900424u

- Beaman, F. D., Bancroft, L. W., Peterson, J. J., Kransdorf, M. J., Menke, D. M., and DeOrto, J. K. (2006). Imaging characteristics of bone graft materials. *Radiographics* 26, 373–388. doi: 10.1148/rg.262055039
- Chandra, V. S., Baskar, G., Suganthi, R. V., Elayaraja, K., Joshy, M. I. A., Beaula, W. S., et al. (2012). Blood compatibility of iron-doped nanosize hydroxyapatite and its drug release. *ACS Appl. Mater. Interfaces* 4, 1200–1210. doi: 10.1021/am300140q
- Chen, F., Huang, P., Zhu, Y. J., Wu, J., Zhang, C. L., and Cui, D. X. (2011). The photoluminescence, drug delivery and imaging properties of multifunctional Eu³⁺/Gd³⁺ dual-doped hydroxyapatite nanorods. *Biomaterials* 32, 9031–9039. doi: 10.1016/j.biomaterials.2011.08.032
- Choi, J. S., Lee, J. H., Shin, T. H., Song, H. T., Kim, E. Y., and Cheon, J. (2010). Self-confirming “AND” logic nanoparticles for fault-free MRI. *J. Am. Chem. Soc.* 132, 11015–11017. doi: 10.1021/ja104503g
- Cipreste, M. F., Peres, A. M., Cotta, A. A. C., Aragon, F. H., Antunes, A. M., Leal, A. S., et al. (2016). Synthesis and characterization of 159Gd-doped hydroxyapatite nanorods for bioapplications as theranostic systems. *Mater. Chem. Phys.* 181, 301–311. doi: 10.1016/j.matchemphys.2016.06.063
- Dou, W., Mastrogiacomio, S., Veltien, A., Alghamdi, H. S., Walboomers, X. F., and Heerschap, A. (2018). Visualization of calcium phosphate cement in teeth by zero echo time 1H MRI at high field. *NMR Biomed.* 31, 3859–3871. doi: 10.1002/nbm.3859
- Getman, E. I., Loboda, S. N., Kachenko, T. V., Yablochkova, N. V., and Chebyshev, K. A. (2010). Isomorphous substitution of samarium and gadolinium for calcium in hydroxyapatite structure. *Russ. J. Inorg. Chem.* 55, 333–338. doi: 10.1134/S0036023610030058
- Habraken, W., Habibovic, P., Epple, M., and Bohner, M. (2016). Calcium phosphates in biomedical applications: Materials for the future? *Mat. Today* 19, 69–87. doi: 10.1016/j.mattod.2015.10.008
- Hoekstra, J. W., Van den Beucken, J. J., Leeuwenburgh, S. C., Bronkhorst, E. M., Meijer, G. J., and Jansen, J. A. (2014). Tantalum oxide and barium sulfate as radiopacifiers in injectable calcium phosphate-poly (lactic-co-glycolic acid) cements for monitoring *in vivo* degradation. *J. Biomed. Mater. Res. A.* 102, 141–149. doi: 10.1002/jbm.a.34677
- Huang, G., Li, H., Chen, J., Zhao, Z., Yang, L., Chi, X., et al. (2014). Tunable T1 and T2 contrast abilities of manganese engineered iron oxide nanoparticles through size control. *Nanoscale* 6, 10404–10412. doi: 10.1039/C4NR02680B
- Liu, Y., Sun, Y., Cao, C., Yang, Y., Wu, Y., Ju, D., et al. (2014). Long term biodistribution *in vivo* and toxicity of radioactive/magnetic hydroxyapatite nanorods. *Biomaterials* 35, 3348–3355. doi: 10.1016/j.biomaterials.2013.12.064
- Madhumathi, K., and Sampath Kumar, T. S. (2014). Regenerative potential and anti-bacterial activity of tetracycline loaded apatitic nanocarriers for the treatment of periodontitis. *Biomed. Mater.* 9:035002. doi: 10.1088/1748-6041/9/3/035002
- Madhumathi, K., Sampath Kumar, T. S., Mohammed Sanjeed, T., Sabik Muhammed, A., Nazrudeen, S., and Sharanya, D. (2014). Silver and gadolinium ions co-substituted hydroxyapatite nanoparticles as bimodal contrast agent for medical imaging. *Bioceram. Dev. Appl.* 4, 1–4. doi: 10.4172/2090-5025.1000079
- Mastrogiacomio, S., Dou, W., Koshkina, O., Boerman, O. C., Jansen, J. A., Heerschap, A., et al. (2017). Perfluorocarbon/gold loading for noninvasive *in vivo* assessment of bone fillers using ¹⁹F magnetic resonance imaging and computed tomography. *ACS Appl. Mater. Interfaces* 9, 22149–22159. doi: 10.1021/acsami.7b04075
- Nakamura, M., Oyane, A., Kuroiwa, K., Shimizu, Y., Pyatenko, A., Misawa, M., et al. (2018). Facile one-pot fabrication of calcium phosphate-based composite nanoparticles as delivery and MRI contrast agents for macrophages. *Colloids Surf. B Biointerfaces* 162, 135–145. doi: 10.1016/j.colsurfb.2017.11.034
- Qi, C., Lin, J., Fu, L. H., and Huang, P. (2018). Calcium-based biomaterials for diagnosis, treatment, and theranostics. *Chem. Soc. Rev.* 47, 357–403. doi: 10.1039/C6CS00746E
- Ramanathan, C., and Ackerman, J. L. (1999). Quantitative solid-state NMR imaging of synthetic calcium phosphate implants. *Magn. Reson. Med.* 41, 1214–1220. doi: 10.1002/(SICI)1522-2594(199906)41:6<1214::AID-MRM18>3.0.CO;2-H
- Ramesh babu, N., Sampath Kumar, T. S., Prabhakar, T. G., Sastry, V. S., and Murthy, K. V. (2007). Antibacterial nanosized silver substituted hydroxyapatite: Synthesis and characterization. *J. Biomed. Mater. Res. A* 80, 581–591. doi: 10.1002/jbm.a.30958
- Sampath Kumar, T. S., and Madhumathi, K. (2016a). “Antibacterial potential of bioceramics used as nanocarriers,” in *Handbook of Bioceramics and Biocomposites*, ed I. V. Antoniac (Cham: Springer), 1333–1373. doi: 10.1007/978-3-319-12460-5_58
- Sampath Kumar, T. S., and Madhumathi, K. (2016b). Antibiotic delivery by nanobioceramics. *Ther. Deliv.* 7, 573–588. doi: 10.4155/tde-2016-0025
- Sampath Kumar, T. S., Madhumathi, K., Rubaiya, Y., and Doble, M. (2015). Dual mode antibacterial activity of ion substituted calcium phosphate nanocarriers for bone infections. *Front. Bioeng. Biotechnol.* 3:59. doi: 10.3389/fbioe.2015.00059
- Shin, T. H., Choi, Y., Kim, S., and Cheon, J. (2015). Recent advances in magnetic nanoparticle-based multi-modal imaging. *Chem. Soc. Rev.* 44, 4501–4516. doi: 10.1039/C4CS00345D
- Siddharthan, A., Seshadri, S. K., and Sampath Kumar, T. S. (2004). Microwave accelerated synthesis of nanosized calcium deficient hydroxyapatite. *J. Mater. Sci. Mater. Med.* 15, 1279–1284. doi: 10.1007/s10856-004-5735-3
- Sun, Y., Ventura, M., Oosterwijk, E., Jansen, J. A., Walboomers, X. F., and Heerschap, A. (2013). Zero echo time magnetic resonance imaging of contrast-agent-enhanced calcium phosphate bone defect fillers. *Tissue Eng. Part C Methods* 19, 281–287. doi: 10.1089/ten.tec.2011.0745
- Tampieri, A., D’Alessandro, T., Sandri, M., Sprio, S., Landi, E., Bertinetti, L., et al. (2012). Intrinsic magnetism and hyperthermia in bioactive Fe-doped hydroxyapatite. *Acta Biomater.* 8, 843–851. doi: 10.1016/j.actbio.2011.09.032
- Tanomaru-Filho, M., Morales, V., Da Silva, G. F., Bosso, R., Reis, J. M. S. N., Duarte, M. A. H., et al. (2012). Compressive strength and setting time of MTA and Portland cement associated with different radiopacifying agents. *ISRN Dent.* 2012, 898051–898055. doi: 10.5402/2012/898051
- Tseng, Y. C., Xu, Z., Guley, K., Yuan, H., and Huang, L. (2014). Lipid-calcium phosphate nanoparticles for delivery to the lymphatic system and SPECT/CT imaging of lymph node metastases. *Biomaterials* 35, 4688–4698. doi: 10.1016/j.biomaterials.2014.02.030
- Uskokovic, V., and Uskokovic, D. P. (2011). Nanosized hydroxyapatite and other calcium phosphates: Chemistry of formation and application as drug and gene delivery agents. *J. Biomed. Mater. Res. Appl. Biomater.* 96B, 152–191. doi: 10.1002/jbm.b.31746
- Vallet-Regi, M., and Gonzalez-Calbet, J. M. (2004). Calcium phosphates as substitution of bone tissues. *Prog. Solid State Chem.* 32, 1–31. doi: 10.1016/j.progsolidstchem.2004.07.001
- Ventura, M., Sun, Y., Cremers, S., Borm, P., Birgani, Z. T., Habibovic, P., et al. (2014). A theranostic agent to enhance osteogenic and magnetic resonance imaging properties of calcium phosphate cements. *Biomaterials* 35, 2227–2233. doi: 10.1016/j.biomaterials.2013.11.084
- Ventura, M., Sun, Y., Rusu, V., Laverman, P., Borm, P., Heerschap, A., et al. (2013). Dual contrast agent for computed tomography and magnetic resonance hard tissue imaging. *Tissue Eng. C* 19, 405–416. doi: 10.1089/ten.tec.2012.0007
- Wang, X., Ye, J., and Wang, Y. (2007). Influence of a novel radiopacifier on the properties of an injectable calcium phosphate cement. *Acta Biomater.* 3, 757–763. doi: 10.1016/j.actbio.2007.01.004
- Wichlas, F., Seebauer, C. J., Schilling, R., Rump, J., Chopra, S. S., Walter, T., et al. (2012). A signal-inducing bone cement for magnetic resonance imaging-guided spinal surgery based on hydroxyapatite and polymethylmethacrylate. *Cardiovasc. Intervent. Radiol.* 35, 661–667. doi: 10.1007/s00270-011-0192-0
- Wu, Y., Chesler, D. A., Glimcher, M. J., Garrido, L., Wang, J., Jiang, H. J., et al. (1999). Multinuclear solid-state three-dimensional MRI of bone and synthetic calcium phosphates. *Proc. Natl. Acad. Sci. U.S.A.* 96, 1574–1578. doi: 10.1073/pnas.96.4.1574

Conflict of Interest Statement: The authors declare that the research was conducted in the absence of any commercial or financial relationships that could be construed as a potential conflict of interest.

Copyright © 2019 Kalidoss, Yunus Basha, Doble and Sampath Kumar. This is an open-access article distributed under the terms of the Creative Commons Attribution License (CC BY). The use, distribution or reproduction in other forums is permitted, provided the original author(s) and the copyright owner(s) are credited and that the original publication in this journal is cited, in accordance with accepted academic practice. No use, distribution or reproduction is permitted which does not comply with these terms.